Chinese Chemical Letters 33 (2022) 2669–2676

Contents lists available at ScienceDirect

Chinese Chemical Letters

journal homepage: www.elsevier.com/locate/cclet

In-situ formed hierarchical transition metal oxide nanoarrays with rich antisite defects and oxygen vacancies for high-rate energy storage devices

Teng Wang[a,b,1,*], Bo Xu[c,1], You Wang[a], Jiaqi Lei[a], Wenjing Qin[c], Ke Gui[b], Chuying Ouyang[c], Kai-Jie Chen[a,*], Hongxia Wang[b,*]

[a] *Key Laboratory of Special Functional and Smart Polymer Materials of Ministry of Industry and Information Technology, Xi'an Key Laboratory of Functional Organic Porous Materials, Department of Chemistry, School of Chemistry and Chemical Engineering, Northwestern Polytechnical University, Xi'an 710072, China*

[b] *School of Chemistry and Physics, Faculty of Science, Queensland University of Technology, Brisbane, QLD 4001, Australia*

[c] *Department of Physics, Laboratory of Computational Materials Physics, Jiangxi Normal University, Nanchang 330022, China*

ARTICLE INFO

Article history:
Received 13 August 2021
Revised 15 September 2021
Accepted 30 September 2021
Available online 3 October 2021

Keywords:
Transition metal oxides
In-situ transformation
Oxygen vacancy
Antisite defects
High-rate
Hybrid supercapacitors

ABSTRACT

Developing transition metal oxides (TMOs) with high energy, power, and long cycle lifetime for electric energy storage devices remains a critical challenge to date. Herein, we demonstrate a facile method that enables *in-situ* transformation of nickel cobalt oxide nanowire arrays (NiCoO NWA) into hierarchical nanowire-nanosheet arrays (ac-NiCoO NWSA) for enhanced energy storage properties. More specifically, the method leads to formation of atomically thin nanosheets (only 2.0 nm) and creates abundant antisite defects and oxygen vacancies. Owing to these merits, the as-prepared ac-NiCoO NWSA electrode exhibits over five-fold higher specific capacity, superior rate capability (up to 100 A/g), and excellent cycling stability of 10,000 cycles at 50 A/g in alkaline electrolyte compared to pristine NiCoO NWA. Density functional theory (DFT) simulations elucidate the electrochemical activity enhancement mechanism of the TMOs. Moreover, our method triggers similar structural reconstruction phenomenon on other TMOs including ZnCo-, CoMn- and ZnNiCo-oxides, proving the universality of the method. Our findings provide a general method towards simultaneously manipulating the micro-morphologies and defects of TMOs for advanced energy storage devices.

Earth-abundant transition metal oxides (TMOs, M = Ni, Co, Fe, *etc.*) have been regarded as promising battery-type electrode materials for high performance electric energy storage devices such as aqueous rechargeable alkaline batteries, supercapacitors (SCs), and Li-ion batteries owing to their safety, low cost, easy fabrication, and high theoretical specific capacity thanks to the faradaic charge storage mechanism [1–3]. Although reports of using these TMOs as pseudocapacitive electrodes for SCs have been widely reported, it is now clear that their electrical energy storage mechanism belongs to batteries [4–6]. Nevertheless, their poor electrical conductivity, sluggish redox reaction kinetics, and irreversible phase change during charge/discharge process often lead to unsatisfactory electrochemical performance such as limited specific capacity, low rate capability, and short charge/discharge cycling lifespan. To remedy these weaknesses, a series of effective synthesis strategies such as engineering material composition, nanostructure, and interface in the device have been proposed [7–11]. Among them, the construction of binder-free electrodes where electrode materials with tailored nanostructure are directly grown on a conductive substrate has demonstrated the effectiveness to enhance the electrochemical performance of the TMO materials due to the benefits of improved interfacial contact and aggregation-free of the nanomaterials during the charge transfer process [12–14]. In particular, arrays with multi-component transition metals and favourable nanostructure can offer high porosity, high specific surface area, efficient charge transport path, and robust structure stability, resulting in excellent electric energy storage property. For example, hierarchical nanostructured arrays including $Co(CO_3)_{0.5}(OH)_x{\cdot}0.11H_2O$@$CoMoO_4$ (CC–CCH@CMO) [15], $NiCo_2O_4$@$CoMoO_4$@Co_3O_4 array [16], Ni-Co-N/$NiCo_2O_4$/GFs [17] and MCo_2O_4@MCo_2S_4@PPy (M = Ni, Zn) sandwich structures

* Corresponding authors.
E-mail addresses: wangt42@nwpu.edu.cn (T. Wang), ckjiscon@nwpu.edu.cn (K.-J. Chen), hx.wang@qut.edu.au (H. Wang).
[1] These authors contributed equally to this work.

https://doi.org/10.1016/j.cclet.2021.09.103
1001-8417/

[18] were reported to exhibit excellent electrochemical performance in terms of specific capacity, rate capability, and cyclability. However, conventional methods for the construction of hierarchical nanostructures often require complex reaction procedures involving multiple reaction steps and delicate controlling of reaction conditions, which makes them unfeasible for practical production on large scale.

Recently, electrochemical methods based on cyclic voltammetry (CV) scanning have been proved easy but effective to induce phase transformation of certain materials into electrochemically favourable material phases for energy storage devices [13,19-25]. Especially, most reports have been focused on transition metal hydroxides owing to their feasible ion intercalation/deintercalation ability [26,27]. For instance, Li *et al.* applied CV to induce hydrogen-vacancy in CoFe layered double hydroxides (LDH), which resulted in enhanced reversible intercalation of a variety of metal ions including Li^+, Na^+, K^+, Ca^{2+}, Mg^{2+} and Zn^{2+} in the LDH, leading to improved energy density [28]. Li *et al.* found that CV cycling induced a phase transition of NiCo carbonate hydroxide (CH) nanowires into oxygen vacancies-enriched NiCo LDH nanosheets [13]. The dramatic crystal phase change and rich defects induced by the electrochemical method are believed to be responsible for the enhanced electrochemical properties of the materials.

To the best of our knowledge, the structural transformation of battery-type multi-metallic oxides based on electrochemical method has not been reported for electrical energy storage applications. Herein, we report a simple electrochemical method to realize the structural transformation of binary nickel cobalt oxide nanowire arrays (NiCoO NWA). More specifically, we have found that CV scanning of NiCoO NWAs in a mild KOH electrolyte bath successfully induced significant surface morphology reconstruction from simple nanowire arrays to nanowire@nanosheet core-shell hierarchical arrays (ac-NiCoO NWSA). The CV activation (CVA) treatment also created rich oxygen vacancies and triggered oxidation of Ni^{2+} and reduction of Co^{3+} to form antisite defects within the spinel phases. Consequently, the as-prepared ac-NiCoO NWSA grown on Ni foam displayed five-fold higher specific capacity than the pristine NiCoO NWA, excellent rate capability at a very high discharge current density up to 100 A/g (suggesting high power density), and extraordinarily long cycling stability at a high current density (> 10,000 charge/discharge cycles at 50 A/g). We performed theoretical simulations based on the density functional theory (DFT) method to elucidate the atomic structural evolution and the underlying mechanism for the enhanced electrochemical activity of the ac-NiCoO NWSA during the CV scanning. The electrochemical performance of the ac-NiCoO NWSA electrode in practical energy storage devices was evaluated by constructing a hybrid supercapacitor (HSC) that used activated carbon (AC) as anode and ac-NiCoO NWSA as cathode. The device delivered excellent energy (31.3 Wh/kg) and power density (17.0 kW/kg), and ultra-long cycling stability (> 20,000 cycles) at a high discharge rate (discharge current density: 10 A/g). We further demonstrated the universality of our method in enhancing electrochemical performance of other battery-type TMOs including ZnCoO NWA, CoMnO NWA, ZnCoO nanosheet array (NSA) and ZnNiCoO NSA. In all these cases, an electrochemically desirable hierarchical nanostructure was formed by using the electrochemical method.

Fig. 1 illustrates the schematics of the synthesis process of the ac-NiCoO NWSA on Ni foam substrate. Briefly, Ni-Co precursor arrays (NiCo PNWAs) were firstly grown on Ni foam substrate through a conventional hydrothermal reaction, which was then annealed at 350 °C in air to produce NiCoO NWA. After this, we exerted 45 CV scans on the NiCoO NWA in a voltage range from −1.0 V to 0.65 V (*vs.* Hg/HgO) under the scanning rate of 20 mV/s in 2 mol/L KOH aqueous solution in a three-electrode configuration to obtain ac-NiCoO NWSA. Compared to previous report which usually activated materials in a positive voltage window, the CV scanning in this work was extended to negative voltage range, which we found is essential to trigger the reorganization of the micro-morphology, oxygen vacancy, and antisite defects in the crystal structure. We also synthesized ac-NiCoO NWSA grown on carbon fiber cloth (CFC) substrate by using the same synthesis procedure except substituting the Ni substrate with a CFC. A similar synthetic strategy was also used for the preparation of nanostructure of other multi-metallic oxides (including ZnCoO NWA, CoMnO NWA, ZnCoO NSA and ZnNiCoO NSA). Details of the synthesis procedure are shown in the experimental section (Supporting information).

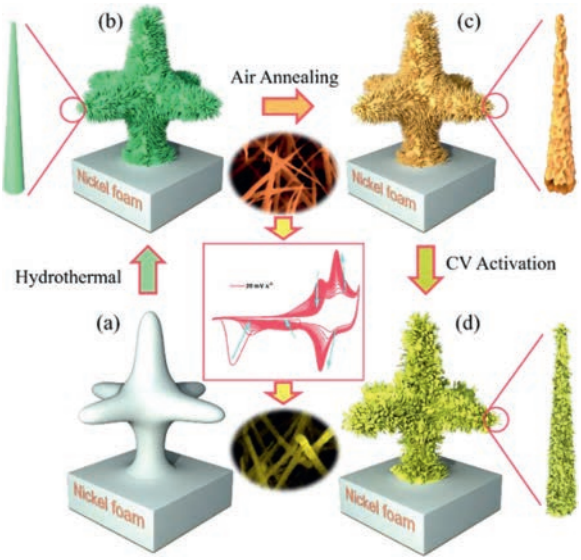

Fig. 1. Schematic illustration of the preparation process of ac-NiCoO NWSA. (a) Ni foam substrate; (b) NiCo PNWA; (c) NiCoO NWA; (d) ac-NiCoO NWSA.

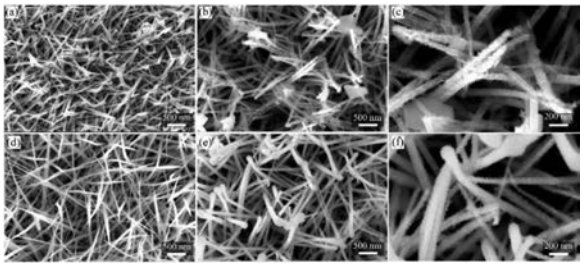

Fig. 2. FESEM images of (a) NiCoO NWA and (b, c) ac-NiCoO NWSA grown on Ni foam. FESEM images of (d) NiCoO NWA and (e, f) ac-NiCoO NWSA grown on CFC substrate.

The morphologies of as-prepared materials were firstly characterized with a field emission scanning electron microscope (FE-SEM). It is seen that the bare Ni foam has a smooth surface (Fig. S1a in Supporting information). After the hydrothermal reaction, it was fully covered by a layer of nanowires (named NiCo PNWA, Figs. S2a-c in Supporting information), which were vertically aligned on the Ni substrate and each wire had a diameter around 50–80 nm. The FESEM images (Fig. 2a) of the NiCoO NWA that was obtained by annealing the NiCo PNWA at 350 °C in air reveal a similar morphological structure to original nanowire arrays. After the CV scanning treatment, a dramatic morphological structure change of the material was observed. All nanowires were evolved into core-shell hierarchical array where each nanowire was coated by numerous ultrathin and small nanosheets, forming nanowire@nanosheet based nano-tree-like heterostructure (Figs. 2b

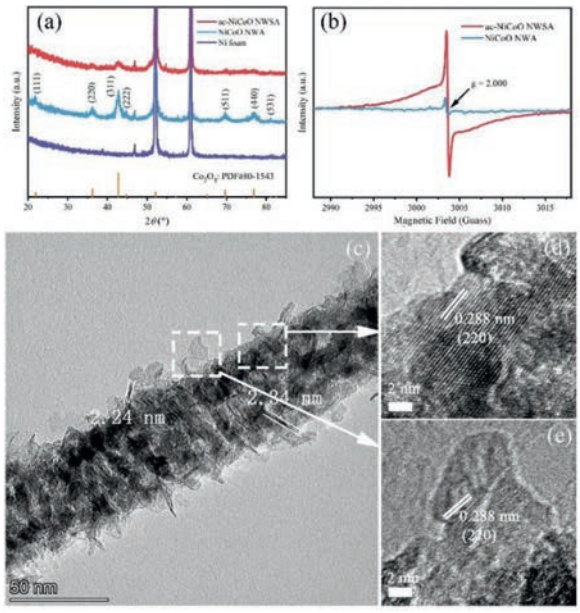

Fig. 3. (a) PXRD patterns of Ni foam substrate, NiCoO NWA, ac-NiCoO NWSA, and the standard spinel structure (Co_3O_4: PDF#80–1543). (b) EPR spectra of NiCoO NWA and ac-NiCoO NWSA grown on CFC substrate. (c) TEM image and (d, e) HRTEM images of ac-NiCoO NWSA.

and c). Considering that the CVA process was undertaken in a pure KOH aqueous solution that did not contain any transition metal ions, the formation of nanosheets during the CV scanning process is ascribed to the surface reconstruction of pristine NiCoO nanowires. The *in situ* formed hybrid structure guarantees an intimate contact between the main nanowire trunk and the nanosheet branches in the tree-like nano-heterostructure. Based on the FE-SEM results, it is believed that the CVA process induced a partial dissolution–recrystallization reaction with the pristine NiCoO NWA, enabling the formation of an ultra-fine sheet substructure directly on the main nanowires backbone. To rule out the influence of Ni foam substrate on the morphology change of NiCoO NWA, we also measured the morphology of NiCoO NWA that was grown on a CFC substrate before and after the CVA process (Figs. 2d-f). The FE-SEM images of bare CFC substrate and CFC coated by NiCo PNWA are shown in Figs. S1b and S3 (Supporting information), respectively. As can be seen, similar to the NiCoO NWA/Ni, pristine NiCoO NWA grown on CFC substrate (Fig. 2d) changed into matchstick-like shape composed of similar nanowire@nanosheet core-shell hierarchical arrays (Figs. 2e and f) after the CVA process. This implies the morphology change of NiCoO NWA is genuinely induced by the CVA process, which is independent of the conductive substrates used.

The crystal structure of as-synthesized materials was determined by powder X-ray diffraction (PXRD). As shown in Fig. 3a and Fig. S4 (Supporting information), except for the characteristic peaks of the Ni foam substrate, all the other diffraction peaks of the pristine NiCoO NWA match well with the diffraction pattern of spinel structure of Co_3O_4 (PDF#80–1543) with a space group of Fd-3 m. Surprisingly, after the CVA treatment, the ac-NiCoO NWSA remained the same crystal structure with the pristine NiCoO NWA although the intensity of the diffraction peaks was seriously damped, suggesting reduced crystallinity of the ac-NiCoO NWSA materials. A similar phenomenon was also found with the ac-NiCoO NWSA grown on CFC (Fig. S5 in Supporting information). This phenomenon differs from all the previous reports in which CVA method induced phase transformation, forming electrochemically favourable new material phases for energy storage applications [24].

We further investigated the micro-morphologies and crystal structure of as-prepared NiCoO NWA and ac-NiCoO NWSA powders that were scraped from the Ni foam substrate by transmission electron microscope (TEM). The TEM images of a nanowire of the NiCoO NWA reveal it is composed of small nanoparticles that are loosely self-assembled together, leading to the formation of a micro-porous structure with pore sizes around 2–5 nm (Fig. S6 in Supporting information). The distinct lattice fringes (0.245 nm and 0.202 nm) observed with the nanowire match well with the (311) and (400) facets of spinel structure (PDF#80–1543, Fig. S6b), which is consistent with the corresponding PXRD results. In contrast, the nanowire of the ac-NiCoO NWSA shows a core-shell heterostructure composed of nanowire core and surface closely packed thin nanosheet shell (Fig. 3c, Figs. S7a and b in Supporting information). The nanosheets possess a small lateral size (< 20 nm) and an ultrathin thickness of only 2.0 nm (Fig. 3c). Fig. 3d depicts the high resolution (HR) TEM image of the core nanowire, which shows lattice fringes with an interplanar spacing of 0.288 nm, corresponding to the (220) facets of spinel structure. The HRTEM image of the nanosheet shell shows blurry lattice fringes of 0.288 nm belonging to the (220) facet (Fig. 3e). This indicates the nanosheets have a much lower crystallinity and/or reduced crystal sizes and more surface defects than the nanowire core. The scanning TEM-high-angle annular dark field (STEM-HAADF) image and the corresponding EDS mapping (Figs. S7b-e in Supporting information) reveal the uniform distribution of Ni, Co, and O elements in the ac-NiCoO NWSA. The chemical composition of the ac-NiCoO NWSA was determined by the EDS spectrum of ac-NiCoO NWSA grown on CFC substrate. It shows the atomic ratio of Co/Ni = 2.08 (Fig. S8 in Supporting information), which is approximate to the value (Co/Ni = 2.17) of pristine NiCoO NWA. This indicates the as-synthesized NiCoO should have a chemical formula of $NiCo_2O_4$ where 1/3 of Co in Co_3O_4 is replaced with Ni. Nevertheless, it is worth pointing out that the PXRD pattern of the NiCoO NWA does not match any of the PDF cards of $NiCo_2O_4$ in the XRD database. This could be due to the existence of significant defects in the material as discussed below.

Analysis of the content of oxygen shows there is a small increase in the Ni/O ratio (from 0.05 to 0.06) and the Co/O ratio (from 0.11 to 0.13) after the CVA treatment according to the EDS results (Fig. S8). The decreased content of oxygen indicates the formation of oxygen vacancies in the metal oxide material induced by the CVA process. To further confirm the exitance of O vacancies, we measured the electron paramagnetic resonance (EPR) spectra of both NiCoO NWA and ac-NiCoO NWSA grown on CFC substrate. As shown in Fig. 3b, no symmetrical signal of O defects was detected for the pristine NiCoO NWA. In contrast, an obvious and strong symmetrical signal at $g = 2.000$ corresponding to unpaired electrons trapped at the position of O vacancies was seen in the EPR spectrum of ac-NiCoO NWSA. This provides solid evidence that the CVA process introduced rich oxygen vacancies in the ac-NiCoO NWSA, which can potentially improve the electrochemical performance of the material.

To further investigate whether the CVA process caused phase change such as the formation of surface amorphous hydroxide/oxyhydroxide species, we compared Raman spectra of the materials (Fig. S10 in Supporting information). The scattering peaks in the Raman spectrum of the NiCoO NWA at 185.6, 461.4, 508.4 and 659.3 cm^{-1} are ascribed to the F_{2g}, E_g, LO and A_{1g} vibrational modes of $NiCo_2O_4$ spinel phases [29,30]. There are no peaks in the region of 3000 – 3750 cm^{-1}, demonstrating the high purity of the metal oxide without water or surface hydroxide group. The Raman spectrum of ac-NiCoO NWSA exhibited similar characteristic Raman scattering peaks but with much lower peak intensity and broader bandwidth in the wavenumber range from 100 cm^{-1} to 800 cm^{-1}, which is ascribed to the reduced crystallinity of the

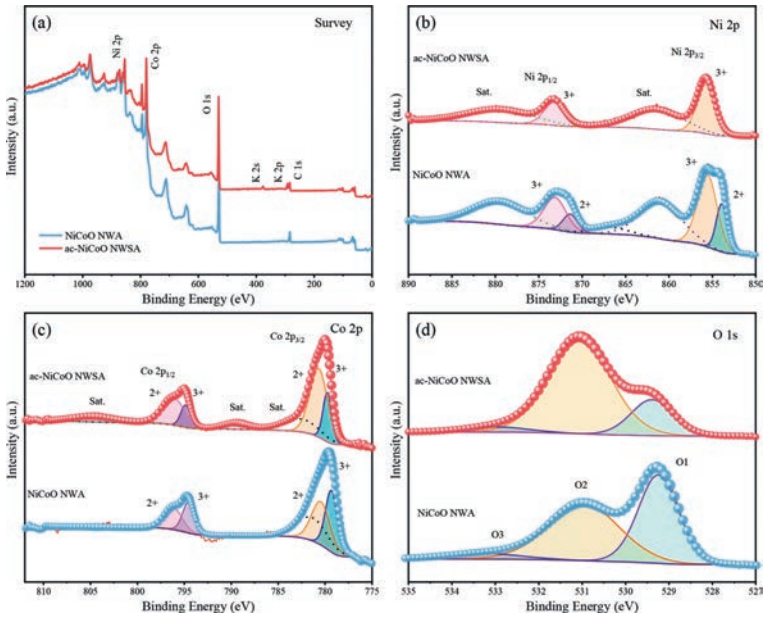

Fig. 4. (a) XPS survey spectra of NiCoO NWA and ac-NiCoO NWSA. XPS spectra comparison of (b) Ni 2p, (c) Co 2p and (d) O 1s in NiCoO NWA and ac-NiCoO NWSA, respectively.

material after CVA process. The above results further confirm the unchanged phase structure of the material during the CVA process.

To further understand the surface properties of the materials, we measured XPS of as-prepared NiCoO NWA and ac-NiCoO NWSA grown on CFC substrates (Fig. 4). The XPS survey spectra (Fig. 4a) show that both materials contain Ni, Co and O elements. The small amount of C should be due to the surface residue. A small amount of K was detected only with the ac-NiCoO NWSA, which is attributed to the K cations of the KOH electrolyte solution adsorbed on the material surface in the CVA step. To investigate the structural evolution, we collected and fitted the XPS spectra of Ni 2p, Co 2p and O 1s spin orbits of both materials. Deconvolution of the XPS spectra of Ni 2p of NiCoO NWA suggests it contains mixed valence states of Ni^{2+} (853.9 eV) and Ni^{3+} (855.7 eV) with the ratio of Ni^{2+}/Ni^{3+}= 0.37 (Fig. 4b) [26]. In contrast, after the CVA, the binding energy of Ni 2p in the ac-NiCoO NWSA shifts positively and all Ni cations in the ac-NiCoO NWSA exist in the form of Ni^{3+} (855.7 eV). The XPS spectra of Co 2p in the NiCoO NWA (Fig. 4c) also suggest a mixed oxidation states of 3+ (779.4 eV) and 2+ (780.6 eV) with the atomic ratio of Co^{2+}/Co^{3+}= 0.69. While, for the ac-NiCoO NWSA, there is a positive shift of a. 0.55 eV in the characteristic binding energy. Deconvolution of the Co 2p spectrum reveals the atomic ratio of Co^{2+}/Co^{3+} = 1.0, confirming a partial reduction of the surface Co^{3+} after the CVA process. The decreased content of Ni^{2+} and the increased content of Co^{2+} after the CVA suggest charge transfer between Ni and Co (Ni^{2+} + Co^{3+} = Ni^{3+} + Co^{2+}). Theoretically, oxidation of Ni^{2+} by Co^{3+} is completely feasible as the electrochemical potential of Co^{3+}/Co^{2+} (1.81 V *vs.* NHE) is much higher than Ni^{3+}/Ni^{2+} (0.49 V *vs.* NHE). Nevertheless, the charge transfer between Ni^{2+} and Co^{3+} does not occur in the $NiCo_2O_4$ material without CVA treatment. It suggests the electrical force in the CVA process drives the charge transfer reaction. The change of the oxidation states of Ni and Co means the shift of their occupying sites in the crystal structure, resulting in abundant antisite defects. Note that this is the first report of the formation of significant antisite defects in transition metal oxides during CVA process. Fitting the XPS spectrum of O 1s (Fig. 4d) reveals three components (O1-O3). The O1 peak located at 529.3 eV corresponds to the typical lattice O^{2-} in the M-O (M = Ni or Co) bonding structure [31]. The weak signal of O3 peak (< 5%) at a. 533.0 eV is due to the surface-adsorbed water molecules or an artefact of fitting asymmetric XPS using symmetric Gaussian functions [32]. The O2 component at 531.0 eV is related to the formation of O–Ni^{3+} bond in the octahedral site and the introduction of oxygen vacancies [33,34]. The proportion of O2 peak increases significantly from 50.4% for the NiCoO NWA to 75.6% for the ac-NiCoO NWSA, which is consistent with the increase of Ni^{3+} and oxygen vacancies as shown above. Although the crystal structure of the NiCoO NWA is largely unchanged after the CVA treatment, the surface chemical properties of the material including rich antisite defects and oxygen vacancies have changed significantly, which is believed to be responsible for the morphology and consequent electrochemical performance change of the material.

In order to evaluate the effect of CVA treatment on electrochemical properties of the materials, we monitored the cyclic voltammetry (CV) plots of the NiCoO NWA grown on Ni foam at different CV scans used in the CVA treatment (as described in experimental section). We notice that conventional CV scanning (positive voltage window: 0 ~0.65 V *vs.* Hg/HgO) only resulted in negligible changes in the electrochemical activity of the NiCoO NWA (Fig. 5a). In order to introduce proper driving forces for the electrochemically structural transformation of pristine NiCoO NWA sample, we expanded the CV potential range to −1.0 ~ 0.65 V. Figs. 5b and c show the evolution of the CV plots of pristine NiCoO NWA grown on Ni foam under the voltage window of −1.0 ~ 0.65 V. As shown in Fig. 5c, the 1st CV plot of NiCoO NWA possesses two reduction peaks at −0.77 V and 0.33 V and three oxidation peaks at 0.09 V, 0.27 V and 0.43 V, respectively. The reduction peak at −0.77 V evolved into two peaks at −0.58 V and −0.12 V at the 2nd CV cycle. As indicated by the blue arrows in Fig. 5b, the redox peaks at 0.43 V and 0.33 V increased continuously along with the increase of CV cycles while the other redox peaks decreased dramatically and eventually disappeared. This proves the NiCoO NWA experienced irreversible redox reactions during the CVA treatment in the voltage range investigated (−1.0 ~ 0.65 V *vs.* Hg/HgO).

To further study the reaction mechanism, we measured the XPS spectra of the Ni and Co 2p spin orbits in the NiCoO NWA at different charge/discharge states (Fig. S11 in Supporting information). We have found that when the pristine NiCoO NWA was firstly discharged to −1.0 V (*vs.* Hg/HgO), the ratio of Ni^{2+}/Ni^{3+} decreased

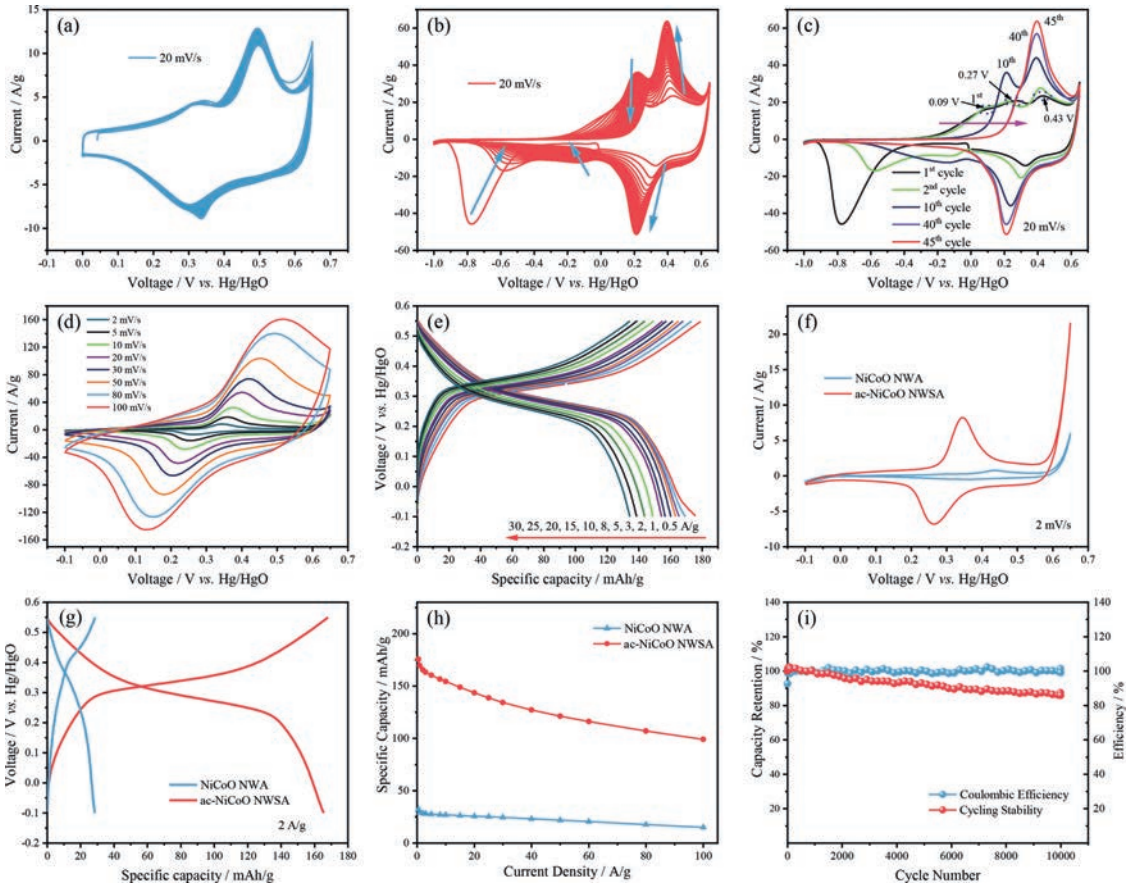

Fig. 5. Electrochemical performance of NiCo-based arrays: CVA process of NiCoO NWA grown on Ni foam showing the evolution of CV activation process in the voltage window of (a) 0 ~ 0.65 V and (b) −1.0 ~ 0.65 V (*vs.* Hg/HgO) at the scanning rate of 20 mV/s, respectively. (c) The extracted 1st, 2nd, 10th and 45th CV cycles showing detailed information of the evolution of CVA process under the voltage window of −1.0 ~ 0.65 V. (d) CV curves at different scan rates and GCD plots at different current densities (e) of ac-NiCoO NWSA. Comparison of (f) CV plots (at 2 mV/s), (g) GCD plots (at 2 A/g) and (h) specific capacity (from 0.5 A/g to 100 A/g) of NiCoO NWA and ac-NiCoO NWSA grown on Ni foam, respectively. (i) Cycling performance of ac-NiCoO NWSA under 50 A/g.

from 0.37 to 0.24, indicating the occurrence of partial oxidation of Ni^{2+}. When the material was recharged to +0.65 V, all of the Ni^{2+} was oxidized to +3 valence state. For Co in the NiCoO NWA, we observed an opposite trend. Specifically, the ratio of Co^{2+}/Co^{3+} increased from 0.69 to 3.24 at −1.0 V. The value was then reduced to 1.37 when the material was recharged to +0.65 V, proving that the Co^{3+} in the NiCoO NWA was reduced at the negative voltage and part of the reduced Co was then re-oxidized at the positive voltage. Based on the XPS results in Fig. 4 and Fig. S11, we can elucidate the evolution of oxidation/reduction peaks in the CV plots in Fig. 5b. Specifically, the reduction peaks of the NiCoO NWA at −0.77 V, −0.58 V and −0.12 V are ascribed to the reduction of Co^{3+} to Co^{2+}. The weak oxidation peak at 0.09 V appearing in the first few CV cycles is the result of oxidation of Ni^{2+} into Ni^{3+}, which disappeared completely when all Ni^{2+} species were oxidized to Ni^{3+}. The oxidation peaks at 0.27 V and 0.43 V should be mainly attributed to the oxidation of Co^{2+} to Co^{3+} and the reduction peak at +0.33 V (which shifts to +0.21 V at 45th CV scan) corresponds to the reduction of Co^{3+}.

We evaluated the electrochemical performance of the materials in a similar three-electrode system. A safe potential window of −0.1 ~ 0.65 V was picked to reveal the full potential of the electrical energy storage capacity of the electrode materials. The distinctive redox reaction peaks in the CV curves (Fig. 5d) and the obvious voltage plateaus in the galvanostatic charge/discharge (GCD) curves (Fig. 5e) of the ac-NiCoO NWSA suggest it adopts a faradaic charge storage mechanism, proving its typical battery-type charge storage behavior [4–6]. The charge/discharge process is mainly related to the reversible redox reactions of Ni and Co cations as shown in Eqs. 1 and 2 [35]:

$$NiCo_2O_4 + OH^- + H_2O \Leftrightarrow NiOOH + CoOOH + e^- \quad (1)$$

$$CoOOH + OH^- \Leftrightarrow CoO_2 + H_2O + e^- \quad (2)$$

Previous reports have also shown Ni^{3+} can be further oxidized to Ni^{4+} during the charge transfer process [36], resulting in higher electric storage capability. The mild shift of the redox peaks in the CV curves of ac-NiCoO NWSA (Fig. 5d) with increased scan rates up to 100 mV/s indicates the material has high electrochemical reversibility, fast electric transportation rate, and excellent rate capability.

Comparison of the CV and GCD plots of the NiCoO NWA and ac-NiCoO NWSA (Figs. 5f and g) under the same condition confirms the superior electrochemical performance of ac-NiCoO NWSA. The specific capacity of the samples was determined based on the GCD results (Fig. 5h). It is found that the ac-NiCoO NWSA delivered a maximum specific capacity of 175.5 mAh/g at 0.5 A/g, which is 5.45 times of the NiCoO NWA (32.2 mAh/g). Even when the discharge current density increased to a very high value of 100 A/g, the ac-NiCoO NWSA still showed a specific capacity of 99.1 mAh/g (meaning a capacity retention rate of 56.5%) which is much higher than that of NiCoO NWA (46.9%), demonstrating its excellent rate capability and high power density. The rate capability of the ac-NiCoO NWSA is superior to most of the state-of-the-art transition metal oxides reported in the literature such as $CoMn_2O_4$ HNSs@Ni

(34.5% from 1 A/g to 13 A/g) [37], $NiCo_2O_4$@NC (29.3% from 5 A/g to 90 A/g) [38], and Co_3O_4–NiO/GF (67.7% from 0.5 A/g to 10 A/g) [39] as shown in Table S1 (Supporting information). Analysis of the electrochemical impedance spectra (EIS) of the materials (Fig. S12 in Supporting information) shows the ac-NiCoO NWSA has smaller series resistance (R_s, R_s = 0.62 Ω/cm^2) and charge transfer resistance (R_{ct}, R_{ct} = 0.33 Ω/cm^2) compared to the NiCoO NWA (R_s = 0.68 Ω/cm^2, R_{ct} = 0.62 Ω/cm^2). The lower R_s and R_{ct} indicate a higher electrical conductivity of the electrode and faster redox reaction kinetics [40], both favoring the electrochemical performance of the material for efficient electrical energy storage. Note that further manipulation of the diameter and length of NiCoO nanowires to optimize the microstructure and change of the Ni/Co ratio in the material can lead to higher electrochemical performance.

Poor cycling stability of battery-type TMOs at high discharge rate (power density) is a well-known bottleneck for their practical applications. To mimic the harsh condition, we measured the cycling stability of the materials at a very large discharge current of 50 A/g. As shown in Fig. 5i, the ac-NiCoO NWSA on Ni foam exhibits a specific capacity retention rate of 87.0% after 10,000 GCD cycling test, confirming its outstanding cycling stability. The capacity retention rate of the ac-NiCoO NWSA at such a large current density is among the highest values reported with transition metal oxides [37-39,41]. The nearly 100% coulombic efficiency during the long-term cycling indicates a high charge transfer efficiency. Moreover, the FESEM images of the ac-NiCoO NWSA after the cycling test show the material remained a core-shell hierarchical array nanostructure (Fig. S13 in Supporting information), proving the robust stability of the material morphological structure. In addition, the cycling performance of ac-NiCoO NWSA under 5 A/g was also measured, which further proves the outstanding cycling stability of the material (Fig. S14 in Supporting information). Compared to the electrochemical properties of other transition metal oxides reported in the literature (Table S1), the ac-NiCoO NWSA in this work indeed possesses superior energy storage ability with outstanding stability.

To get a fundamental understanding of the material's structural evolution process during the CVA process and their correlation with the material's electrochemical properties, we performed theoretical calculations based on the density functional theory (DFT) method to obtain the total energy of the crystal structure of $NiCo_2O_4$ in the presence of oxygen vacancy and electron injection. Since the metal ions in the ac-NiCoO NWSA exhibited the charge states of Ni^{3+} and $Co^{2+/3+}$ while the pristine NiCoO NWA possessed mixed valence states of $Ni^{2+/3+}$ and $Co^{2+/3+}$ in the material, therefore we constructed two typical configurations (based on inverse spinel) of $NiCo_2O_4$ to simulate these two materials. In one configuration (Fig. 6a), Co^{2+} atoms occupy all the 8a sites (tetrahedral sites) while Co^{3+} and Ni^{3+} share the 16d sites (octahedral sites). We named this configuration Ni_{oct}-inv. In the second configuration, both Co and Ni atoms have a mixed tetrahedral-octahedral arrangement to reflect the coexistence of $Ni^{2+/3+}$ and $Co^{2+/3+}$. This configuration is labeled as $Ni_{oct\text{-}tet}$-inv (Fig. 6b). Firstly, we calculated the total energy of Ni_{oct}-inv and $Ni_{oct+tet}$-inv configurations at charge neutrality state. The results show that the energy of $Ni_{oct+tet}$-inv is about 104 meV lower than that of Ni_{oct}-inv (Table S2 in Supporting information), suggesting the Ni atoms prefer to occupy both tetrahedral and octahedral sites, which are consistent with the observations in our experiment that the pristine NiCoO NWA contains both Ni^{2+} and Ni^{3+} ions.

Since abnormal partial oxidation of Ni^{2+} was observed when the NiCoO NWA was firstly discharged to −1.0 V during the CV scanning, which may play a vital role for the structural reconfiguration. To simulate this process, we injected 1.0 electron into the Ni_{oct}-inv and $Ni_{oct+tet}$-inv configurations, respectively, and monitored the total energy of the resultant structures. The results show that the energy of the $Ni_{oct+tet}$-inv is 12 meV higher than that of the Ni_{oct}-inv (Table S2). It infers that Ni atoms prefer to stay at the octahedral sites (Ni^{3+}) after the electron injection to have the lowest energy. Considering the material was discharged to a quite negative voltage condition, we continue to inject 1.0 more electron into the Ni_{oct}-inv and $Ni_{oct+tet}$-inv configurations, respectively. We found the energy difference between the two configurations increases significantly and reaches 144 meV. This further proves that the occupation of octahedral sites is favorable for Ni atoms.

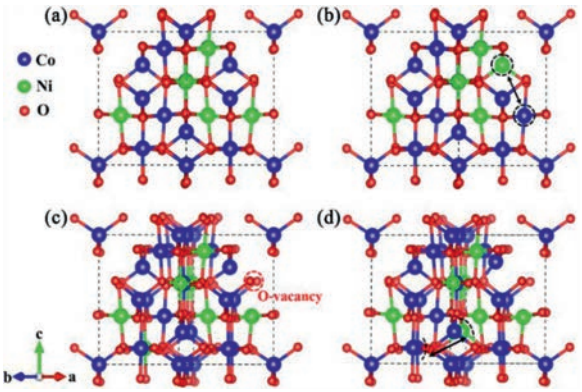

Fig. 6. The atomic structures of (a) Ni_{oct}-inv, (b) $Ni_{oct+tet}$-inv, (c) Ni_{oct}-V_O and (d) $Ni_{oct+tet}$-V_O. The black dotted circles indicate the exchanged octahedral Ni and tetrahedral Co atoms. The red dotted circle indicates the location of oxygen vacancy.

However, the Ni in a high oxidation state (+3) is normally metastable and tends to be reduced to a lower and more stable state, which makes the final ac-NiCoO NWSA unstable thermodynamically. Based on the experimental results of the formation of significant oxygen vacancies during the CVA process, we investigate the effect of oxygen vacancy on the crystal structure of the two configurations by introducing one oxygen vacancy in the Ni_{oct}-inv and $Ni_{oct+tet}$-inv configurations, respectively. They are labeled as Ni_{oct}-Vo and $Ni_{oct+tet}$-Vo (Figs. 6c and d). We found that indeed the energy of the Ni_{oct}-Vo is dramatically reduced, which is 254 meV lower than that of the $Ni_{oct+tet}$-Vo (Table S3 in Supporting information). Therefore, the oxygen vacancies are critical to stabilizing the crystal structure of ac-NiCoO NWSA where all Ni occupies the octahedral sites (Ni^{3+}). The theoretical simulation well explains the crystal structural transformation induced by CVA process.

To understand the correlation of electrochemical activity of the material with crystal structure re-organization, we compared the density of states (DOS) of the Ni_{oct}-inv, $Ni_{oct+tet}$-inv, and Ni_{oct}-V_O (Fig. S15 in Supporting information). It is found that the introduction of oxygen vacancies (Ni_{oct}-V_O) significantly affects the electronic structures of $NiCo_2O_4$, increasing spin-down states around the Fermi level. Generally, the electronic states around the Fermi level can influence the electrochemical activity of the materials significantly. Therefore, the oxygen vacancies introduced by the CVA method are responsible for the observed electrochemical property improvement of the ac-NiCoO NWSA compared to the NiCoO NWA.

Owing to the considerable electric energy storage and high rate charge/discharge capability, ac-NiCoO NWSA should be an ideal candidate as electrode for fabricating high-rate electrical energy storage devices with considerable energy storage capacity. To confirm this hypothesis, we fabricated a hybrid supercapacitor (HSC) by using battery-type ac-NiCoO NWSA (on Ni foam) as cathode, electric double layer capacitive activated carbon (AC) as anode, and 2 mol/L KOH aqueous solution as electrolyte (total active material mass loading: 2.84 mg). As shown in Fig. 7a, the assembled ac-NiCoO NWSA//AC HSC can operate safely in a voltage window of 0-1.7 V without obvious water decomposition. The largely unchanged

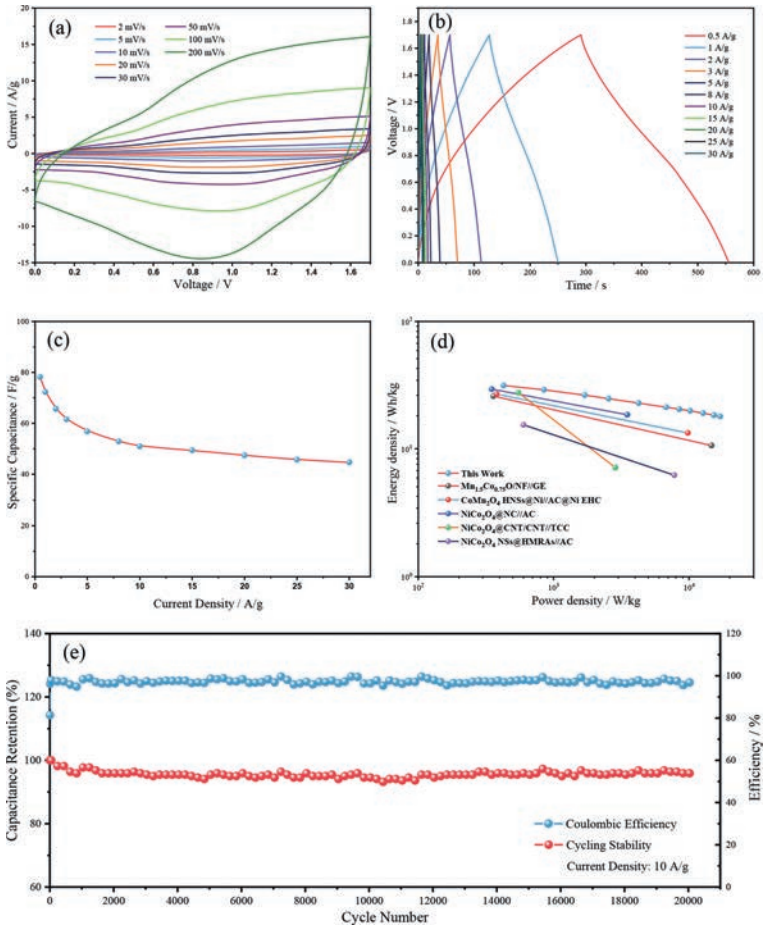

Fig. 7. Electrochemical performance of ac-NiCoO NWSA//AC HSC: (a) CV plots, (b) GCD curves, (c) specific capacity at different current densities, (d) Ragone plot, and (e) cycling stability.

quasi-rectangular shape of the CV plots with a pair of broad redox peaks with increase of the scan rate from 2 mV/s to 200 mV/s demonstrates a mixed capacitive/battery-like charge storage behavior, outstanding reaction reversibility, and excellent rate capability. A small IR drop is noticed in the nearly symmetric triangle GCD plots of ac-NiCoO NWSA//AC HSC at different discharge current densities (0.5–30 A/g), which indicates a capacitive charge storage dominant mechanism (Fig. 7b). The specific capacitance results according to the GCD plots (Fig. 7c) show the as-prepared aqueous HSC delivered a maximum specific capacitance of 78.1 F/g at 0.5 A/g, which remained 44.7 F/g even at 30 A/g, proving the high charge storage ability and outstanding rate capability of the device. The excellent rate capability is attributed to the high rate capacity retention rate of ac-NiCoO NWSA which can keep a good charge balance with capacitive AC at high discharge current density. The Nyquist plot of the EIS spectrum (Fig. S16 in Supporting information) reveals the as-obtained HSC possessed a small R_s (2.05 Ω/cm^2) and R_{ct} (0.93 Ω/cm^2). The Ragone plot (Fig. 7d) shows the HSC exhibited a maximum energy density of 31.3 Wh/kg (at the power density of 427.0 W/kg) and the highest power density of 17.0 kW/kg (at the energy density of 17.9 Wh/kg). The energy storage performance of ac-NiCoO NWSA//AC HSC in this work is comparable or even higher than the state-of-the-art transition metal oxide-based HSCs reported in the literature [37,38,42-44]. More importantly, the cycling stability test of the device based on the ac-NiCoO NWSA reveals over 96% specific capacity retention rate after 20,000 GCD cycles at 10 A/g (Fig. 7e), demonstrating its excellent lifespan at high discharge rate, which outperforms most transition metal oxides based HSCs reported in the literature. A comparison showing systematic electrical energy storage performance of the ac-NiCoO NWSA//AC HSC in this work to other transition metal oxides based HSCs is summarised in Table S4 (Supporting information).

Based on the experimental results shown above, we believe the excellent electrochemical performance of ac-NiCoO NWSA should be ascribed to the following factors: (1) the binder-free electrode design ensures intimate contact between the active material and the conductive substrate for fast electron transportation; (2) the formation of electrochemically favourable core-shell hierarchical nanostructure induced by the electrochemical method ensures high structural stability of the material during high-rate charge/discharge process, and (3) the formation of antisite defects (valence change of Ni and Co) and oxygen vacancies induced by the CVA process generate rich electrochemically active sites for the charge transfer process, leading to a high energy storage capability of the material. We further tested the effectiveness of the CVA with many other binary and even ternary battery-type transition metal oxides including ZnCoO NWA, CoMnO NWA, ZnCoO NSA and ZnNiCoO NSA. All these materials showed improved energy storage capability after the CVA treatment (Fig. S17 in Supporting information), implying the generality of this method. Until now, it is found the TMOs containing Co elements can be electrochemically activated by CVA method, which indicates the critical role of Co elements. Nevertheless, we believe the CVA method should also be applicable to other non-Co based transition metal oxides with proper design of the material composition.

In summary, we realized the *in-situ* structural reconfiguration of battery-type NiCoO NWA into hierarchical ac-NiCoO NWSA using a simple but effective CVA method. The as-prepared ac-NiCoO NWSA grown on Ni foam delivered a significantly enhanced specific capacity of 175.5 mAh/g at 0.5 A/g, superior rate capability (56.5% capacity retention at 100 A/g), and a robust cyclability of over 10 000 GCD cycles (87.0% retention rate) in alkaline electrolyte for electric energy storage applications. The theoretical DFT calculation demonstrated the thermodynamically favourable phase transition process during CVA step and the positive effects of oxygen vacancies for electrochemical performance enhancement of ac-NiCoO NWSA. The excellent electrochemical property of the ac-NiCoO NWSA is attributed to the unique nanowire-nanosheet based nano-tree hierarchical nanostructure and change of surface elemental chemistry (oxygen vacancies and antisite defects). The as-prepared HSC that used the ac-NiCoO NWSA as cathode and activated carbon as anode exhibited high energy density (31.3 Wh/kg), high power density (17.0 kW/kg), and ultralong cycling life of over 20,000 cycles (96.0% retention rate) without significant performance drop. We further demonstrated the university of the CVA method in enhancing electrochemical performance of other battery-type transition metal oxides (ZnCoO NWA, CoMnO NWA, ZnCoO NSA and ZnNiCoO NSA). The structural restructuring reaction mechanism for battery-type transition metal oxides based on our CVA method will benefit the designing of transition metal oxides with controlled micro-morphologies and defects for high-performance electric energy storage devices in the future.

Declaration of competing interest

The authors declare that they have no known competing financial interests or personal relationships that could have appeared to influence the work reported in this paper.

Acknowledgments

This work was supported by National Natural Science Foundation of China (Nos. 21905229, 22071195 and 21805227), China Postdoctoral Science Foundation (No. 2020M683557), Fundamental Research Funds for the Central Universities (No. 3102017jc01001), the postgraduate research scholarship at Queensland University of Technology (QUT-PRA scholarship), and the Youth Innovation Team of Shaanxi Universities. We would like to thank the Analytical & Testing Center of Northwestern Polytechnical University (NPU) for collecting the characterization data (FESEM and XPS data) for us.

Supplementary materials

Supplementary material associated with this article can be found, in the online version, at doi:10.1016/j.cclet.2021.09.103.

References

[1] C. Yuan, H.B. Wu, Y. Xie, X.W. Lou, Angew. Chem. Int. Ed. 53 (2014) 1488–1504.
[2] X. Yuan, F. Ma, L. Zuo, et al., Electrochem. Energy Rev. 4 (2020) 1–34.
[3] J. Jiang, Y. Li, J. Liu, et al., Adv. Mater. 24 (2012) 5166–5180.
[4] Y. Gogotsi, R.M. Penner, ACS Nano 12 (2018) 2081–2083.
[5] T. Brousse, D. Bélanger, J.W. Long, J. Electrochem. Soc. 162 (2015) A5185–A5189.
[6] P. Simon, Y. Gogotsi, B. Dunn, Science 343 (2014) 1210–1211.
[7] T. Wang, H.C. Chen, F. Yu, et al., Energy Storage Mater. 16 (2019) 545–573.
[8] M.R. Lukatskaya, B. Dunn, Y. Gogotsi, Nat. Commun. 7 (2016) 12647.
[9] J. Yan, Q. Wang, T. Wei, Z. Fan, Adv. Energy Mater. 4 (2014) 1300816.
[10] J. Mei, T. Liao, G.A. Ayoko, et al., Prog. Mater Sci. 103 (2019) 596–677.
[11] M. Huang, M. Li, C. Niu, et al., Adv. Funct. Mater. 29 (2019) 1807847.
[12] M. Zhou, Y. Xu, Y. Lei, Nano Today 20 (2018) 33–57.
[13] S. Li, Y. Zhang, N. Liu, et al., Joule 4 (2020) 673–687.
[14] J. Qi, Y. Yan, Y. Cai, et al., Adv. Funct. Mater. 31 (2020) 2006030.
[15] M. Li, J. Meng, Q. Li, et al., Adv. Funct. Mater. 28 (2018) 1802016.
[16] Y. Xie, B. Fei, D. Cai, et al., Energy Storage Mater. 31 (2020) 27–35.
[17] H. Tan, Z. Liu, D. Chao, et al., Adv. Energy Mater. 8 (2018) 1800685.
[18] D. Zhao, H. Liu, X. Wu, Nano Energy 57 (2019) 363–370.
[19] X. Ji, S. Cheng, L. Yang, et al., Nano Energy 11 (2015) 736–745.
[20] Y. Yu, Y. Tan, B. Yang, et al., J. Power Sources 443 (2019) 227278.
[21] H. Chen, Y. Kang, F. Cai, et al., J. Mater. Chem. A 3 (2015) 1875–1878.
[22] W. Xu, T. Wang, H. Wang, et al., Energy Storage Mater. 17 (2019) 300–308.
[23] X. Wang, Z. Zhou, Z. Sun, et al., Nano-Micro Lett. 13 (2020) 4.
[24] N. Jabeen, A. Hussain, Q. Xia, et al., Adv. Mater. 29 (2017) 1700804.
[25] Q. Gou, S. Zhao, J. Wang, et al., Nano-Micro Lett. 12 (2020) 98.
[26] T. Wang, F. Yu, X. Wang, et al., Electrochim. Acta 334 (2020) 135586.
[27] Z.-.H. Huang, F.F. Sun, Z.Y. Yuan, et al., Nano Energy 82 (2021) 105727.
[28] Z. Li, H. Duan, M. Shao, et al., Chem 4 (2018) 2168–2179.
[29] A.K. Das, R.K. Layek, N.H. Kim, et al., Nanoscale 6 (2014) 10657–10665.
[30] D. Li, Y. Gong, Y. Zhang, et al., Sci. Rep. 5 (2015) 12903.
[31] Y. Lu, W. Zhan, Y. He, et al., ACS Appl. Mater. Interfaces 6 (2014) 4186–4195.
[32] J.G. Kim, D.L. Pugmire, D. Battaglia, M.A. Langell, Appl. Surf. Sci. 165 (2000) 70–84.
[33] L. Huang, W. Zhang, J. Xiang, Y. Huang, J. Materiomics 2 (2016) 248–255.
[34] H.-.Y. Wang, Y.-.Y. Hsu, R. Chen, et al., Adv. Energy Mater. 5 (2015) 1500091.
[35] T. Wang, S. Zhang, X. Yan, et al., ACS Appl. Mater. Interfaces 9 (2017) 15510–15524.
[36] J.H. Lee, H.J. Lee, S.Y. Lim, et al., Adv. Funct. Mater. 27 (2017) 1605225.
[37] S.K. Hussain, G. Nagaraju, S.Chandra Sekhar, J.S. Yu, Energy Storage Mater. 27 (2020) 405–417.
[38] Z. Xu, J. Ren, Q. Meng, et al., ACS Sustainable Chem. Eng. 7 (2019) 12447–12456.
[39] P. Wang, H. Zhou, C. Meng, et al., Chem. Eng. J. 369 (2019) 57–63.
[40] T. Wang, Y. Wang, J. Lei, et al., Ceram. Int. 46 (2020) 22934–22943.
[41] Z. Qu, M. Shi, H. Wu, et al., J. Power Sources 410-411 (2019) 179–187.
[42] G. Li, M. Chen, Y. Ouyang, et al., Appl. Surf. Sci. 469 (2019) 941–950.
[43] P. Wu, S. Cheng, M. Yao, et al., Adv. Funct. Mater. 27 (2017) 1702160.
[44] X.F. Lu, D.J. Wu, R.Z. Li, et al., J. Mater. Chem. A 2 (2014) 4706–4713.